Energetics of Hurricane Bonnie (1998)

Wallace Hogsett

Department of Atmospheric and Oceanic Science, University of Maryland
College Park, Maryland 20742

Submitted as M.S. Scholarly Paper

December 2006

Abstract

A real-data simulation of Hurricane Bonnie (1998) is analyzed diagnostically from an energetics point of view. Budgets and structure of the mean and perturbation kinetic energy (KE), as well as latent energy (LE), are shown using equations derived for the MM5 system. Early in this case study, Bonnie intensifies under the influence of vertical shear, which causes the reflectivity and KE structure to take on a wavenumber-1 asymmetry. The structure of the storm changes quickly and dramatically as the influence of vertical shear lessens, and the vortex undergoes an eyewall replacement and azisymmetrization prior to landfall. Vertical shear is the underlying source of the significant asymmetries in Bonnie.

The energetic processes which lead to the development of the asymmetries and the subsequent axisymmetrization (coincident with the decay of asymmetries) are explored, and it is found that the asymmetries initiate in the lower troposphere at the eye-eyewall interface and propagate outward with time. As the asymmetries propagate outward as rainbands, they facilitate the decay of the main eyewall and set the stage for axisymmetrization, which occurs in the absence of significant eddy processes.

1. Introduction

Tropical cyclones (TCs) can devastate life and property, and the associated total damage is positively correlated with the amount of kinetic energy (KE) contained within the storm. McBride (1981) mentions that most life and property loss occurs within a one degree radius of the storm center, roughly the same location as the highest values of KE causing the damage. TCs develop and maintain great amounts of KE through a continuous series of energy conversions, with the latent energy (LE) as the fundamental source.

TCs obtain the requisite sensible and latent energy through upward heat fluxes and evaporation of vapor from the underlying warm ocean and release it in convective clouds in the eyewall. Some of the released LE is then converted to KE. The location and quantity of such energy transformations dictate the intensification rate of the cyclone. Thus, the relationship between LE and KE is important to the understanding of TC evolution.

Observational and modeling studies have been conducted to gain insight into the budgets of KE and LE. Frank (1977) used compositing rawinsondes to calculate KE and moist static energy budgets of TCs and showed how TCs import KE from their environment and produce most KE in the near-surface layer. McBride (1981) composited data from both the Atlantic and Pacific basins to calculate energy budgets for different tropical cloud clusters, which were partitioned into those which intensified into TCs and those that did not. It was found that intensifying storms are characterized by a synoptic scale increase in KE and sensible heat, but a decrease in LE. Additionally, the KE budget residual indicates the requirement for eddy KE generation, and deep convection embedded in a vertically sheared environment was suggested as a possible source. Both studies showed the structure of energy processes in TCs, but they were limited by the poor resolution of observations from peering into the processes of an individual storm.

Vincent et al. (1974) utilized the land-based surface and rawinsonde observations to calculate the KE budget of Hurricane Celia (1970) after landfall in Texas. They found that the storm maintained constant system-integrated KE up to 24 hours after landfall. During this time, the generation of KE was positive, and there was a net import of KE into the system. As the storm weakened, the generation of KE became negative, and the storm began to export KE. The land-based nature of the study as well as data resolution limits the degree to which the findings can be applied to other TCs.

Vincent et al. (1974) also mentioned a need for a storm-following coordinate system to investigate TCs. Such a quasi-Lagrangian methodology can only be utilized when high resolution data along a significant length of the TC trajectory is available. The relative lack of data in the tropical oceans thus limits the depth to which observational studies can capture the energetic processes of TCs.

However, the ability of mesoscale models to reproduce TCs and provide dense, high-quality data is continually increasing. Models have evolved from axisymmetric models (e.g., Kasahara, 1961; Ooyama, 1969) in the 1960s that were able to produce basic TC features and circulations, to coarsely resolved three-dimensional (3D) models that parameterized convection. For example, Tuleya and Kurihara (1975), hereafter TK75, used the GFDL TC model to simulate an idealized TC, and they calculated budgets of mean and eddy KE, as well as LE. They found that the KE budgets are determined primarily by the mean flow, although the contribution of eddies is not negligible, and that the features of the mean flow agree well with both observational and modeling studies. More recently, Wang (2002) analyzed the inner core of an idealized simulated TC to show the structure of eddy KE, as well as the energetic processes that contribute to the formation of vortex Rossby waves. It was found that the maxima in the eddy KE occur in the lower levels near the RMW and in the upper level outflow layer. The largest contributions to the production of eddy KE were a conversion from potential energy and conversion from the azimuthal mean KE.

Comparisons between the quantitative aspects of various studies are difficult to rationalize due to the differences in the actual storm structure, size of the domain considered, and external influences. For example, neither Wang (2002) nor TK75 considered the effect of environmental flow on the energetic processes of the storm. However, it is useful to address the relative importance of physical processes in the maintenance of KE and in the development of asymmetries.

Recently, mesoscale models have been successfully used to simulate real hurricanes (e.g., Liu et al. 1997, Braun 2002, Zhu et al. 2004). Not only do these simulations produce the correct track and intensity evolution, they also reproduce well the intricate inner-core structures as observed by radar and in-situ observations. In fact, the simulation of Hurricane Andrew (1992) by Liu et al. (1997) was able to reproduce the small scale return outflow that has been observed (Barnes and Powell, 1995) to occur just above the boundary layer inflow in another mature TC. Mesoscale models have reached the point where they can be used to confidently investigate the inner core dynamics, including energetic processes, of individual storms.

Recently, Zhu et al. (2004), hereafter referred to as ZZW, took yet another step toward a realistic simulation of a TC by incorporating satellite-derived winds, as well as daily-updated sea surface temperatures into an explicit simulation of Hurricane Bonnie (1998). The observed Bonnie exhibited variations in eyewall structure and fluctuations in intensity throughout her lifetime, and ZZW realistically reproduced these characteristics with the finest grid resolution of 4 km.

The availability of this high spatial and temporal resolution data facilitates a detailed energy study of a real TC. Analyzing the inner core energetic processes of a real TC will provide insight into the location and importance of the physical processes that lead to intensification. With such a high resolution dataset, not only the processes that act to intensify the storm can be brought to light, but also the evolution of the asymmetric processes that are important for modulation of TC intensity can be discussed.

The case of Hurricane Bonnie (1998) will be examined by performing Lagrangian budget analyses using the ZZW simulation. The purposes of the current study are to a) examine the temporal evolution and 3D structures of KE and LE, b) calculate budgets of both total LE and total KE, c) provide insight into the evolution and 3D structures of conversion processes that link the energies, d) calculate the budget of eddy KE, and e) analyze the 3D structures of the important terms in the eddy KE budget.

The next section provides a brief review of Hurricane Bonnie and the simulation. Section 3 presents the budget equations used for the study. Section 4 provides a look at the evolution and structure of KE and LE as well as a time series of budget terms throughout the lifetime of Bonnie. Section 5 delves into the structure of the energy conversion processes. Section 6 will address the mean and eddy budgets of KE and analyze the structure of important terms in the budgets, and the final section gives a summary and concluding remarks.

2. Overview of Hurricane Bonnie

Bonnie developed near the west coast of Africa, and after an eight-day development period it reached hurricane status on 22 August 1998. Upon entering a favorable upper level environment shortly after reaching category 1 status, it deepened rapidly for the next 48 hours and reached its minimum pressure on 24 August. After weakening slightly, Bonnie maintained its intensity, with a slight fluctuation related to an eyewall replacement cycle, for the next three days.

Superimposed on the intensity variation, characterized simply by a rapid intensification at the early stage and a subsequent maintenance stage, is a structural evolution of the eyewall. Airborne radar observations show that the eyewall was highly asymmetric during 22 to 25 August – a period of rapid intensification. Then, the eyewall evolved, after a "partial" eyewall replacement, into a more axisymmetric structure during 25 - 27 August. ZZW explained the structural variability in terms of vertical wind shear that was strongest during the partial eyewall stage. They explained that the highest reflectivity, characterized by a wavenumber-1 asymmetry early in Bonnie's lifetime, occurs to the downshear-left of the shear vector.

ZZW provided an explicit, real-data, triply nested MM5 simulation of Hurricane Bonnie that agrees quite well with observations of both structure and intensity. Fig. 1 shows the rapid deepening from 36 - 48 h and subsequent weakening and reintensification from 36 – 96 h that is evident in the evolution of minimum pressure and maximum surface wind, for the simulated Bonnie. Fig. 2 shows the evolution of eyewall structure, including the shear-forced wavenumber-1 asymmetry that intensifies in the northeast quadrant until 48 h and remains until 65 h, after which the azimuthal coverage of reflectivity increases in association with axisymmetrization. See ZZW for a more detailed case description. In this study, we will utilize data from the finest mesh of 4 km at both 15-min and 3-hourly output intervals.

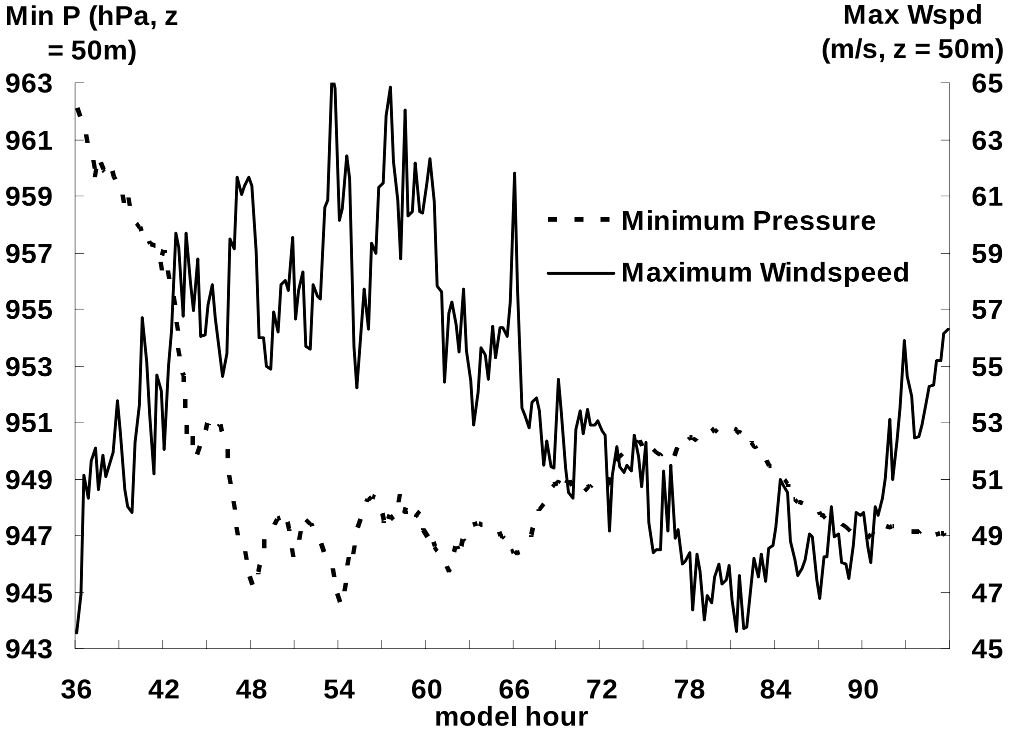

Figure 1: Time series (15 m) of the minimum central pressure (dashed, hPa) and the maximum near-surface winds (solid, m/s) from the model simulation.

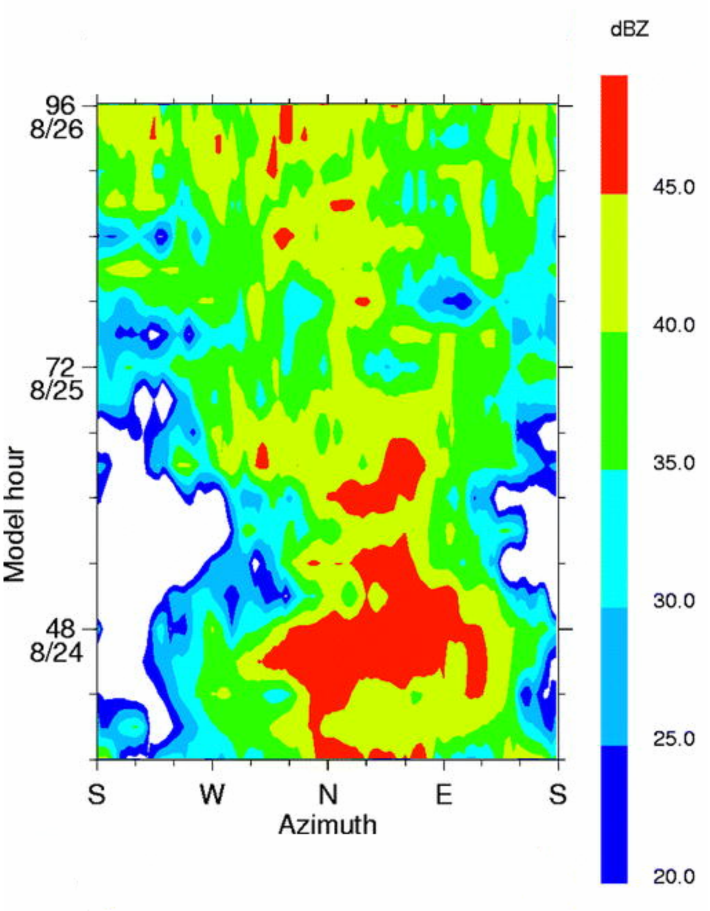

Figure 2: Time-azimuth cross section of the simulated radar reflectivity along the updraft core at z = 5 km. From Zhu et al. (2004)

3. Energy Equations

In this chapter, prognostic equations for KE, LE, total potential energy (TPE), as well as the total energy (TE) for the MM5 system are presented. Details of the non-hydrostatic MM5 equation system can be found in Dudhia (1993). The budget equations that will follow are presented in the quasi-Lagrangian framework, where the left hand side of the equations contains both local tendency and changes of the quantity due to domain translation. Various energies per unit volume are defined as follows:

$$KE = \rho \frac{\vec{V}_h \bullet \vec{V}_h}{2}$$

$$TPE = \rho(c_v T + gz) = IE + PE$$

$$LE = \rho L_v q_v$$

$$TE = KE + TPE + LE$$

where V_h is the horizontal velocity vector with respect to the ground. The vertical component of KE, $w^2/2$, is not included because it is one to two orders of magnitude smaller than the horizontal component. The units of each energy are J m^{-3}.

The KE equation can be obtained by taking the dot product of the MM5 horizontal momentum equation with the horizontal velocity vector:

$$\frac{d}{dt}(KE) = -\vec{V}_H \bullet \nabla p' - \vec{V} \bullet \vec{F} \tag{3.1}$$

Thus, sources and sinks of KE are associated with horizontal cross-isobaric flows and friction. Friction includes the boundary layer processes, such as both vertical and horizontal diffusion. When (3.1) is volume integrated, another term representing the import of KE at the lateral boundaries arises (Dutton, 1976).

The IE equation in the MM5 system can re-written as:

$$\frac{d}{dt}(IE) = -p\nabla \bullet \vec{V} + \rho \frac{c_v}{c_p} L_v (Q_{con} - Q_{ev}) + SHF \tag{3.2}$$

where Q_{con} and Q_{ev} represent the vapor mixing ratio tendencies due to the processes of condensation and evaporation, respectively. In this formulation, we calculate the $L_v(Q_{con} - Q_{ev})$ term as the heating rate $\frac{c_p}{\pi}\frac{d\theta}{dt}$, where $\pi = (\frac{p_0}{p})^{R/c_p}$ and the total derivative is approximated as $\frac{d\theta}{dt} \approx (\vec{V} - \vec{C}) \bullet \nabla\theta$, where C is the horizontal storm motion vector and the del operator is the three-dimensional gradient. Radiation is absorbed into the calculation, but latent heat release dominates the heating rate. The SHF term represents a source of IE due to sensible heat flux from the ocean and land surface into the atmosphere.

In order to maintain consistency with (3.1), (3.2) can be rewritten as:

$$\frac{d}{dt}(IE) = -\nabla \cdot (p\vec{V}) + \vec{V} \cdot \nabla p + \rho L_v (Q_{con} - Q_{ev}) + SHF \tag{3.3}$$

where the first term on the right hand side vanishes when periodic lateral boundary conditions are used. However, it must be included for this regional budget study.

The PE equation is derived by taking the time derivative of the definition of geopotential:

$$\frac{d}{dt}(PE) = \rho g w \tag{3.4}$$

Adding (3.3) and (3.4) yields the TPE equation:

$$\frac{d}{dt}(TPE) = -\nabla \cdot (p\vec{V}) + \vec{V} \cdot \nabla p + \rho g w + \rho L_v (Q_{con} - Q_{ev}) + SHF \tag{3.5}$$

In order to maintain consistency with the KE equation, we remove from Eqn. (3.5) the hydrostatic base state:

$$-w\frac{\partial p_0}{\partial z} - \rho_0 g w = 0,$$

which yields a complete equation for total potential energy:

$$\frac{d}{dt}(TPE) = -\nabla \cdot (p\vec{V}) + \vec{V}_H \cdot \nabla p' + \rho L_v (Q_{con} - Q_{ev}) + SHF \tag{3.6}$$

Finally, in order to complete the inventory of energies and account for the crucial component for TC development and maintenance, we present an equation for LE. This equation is obtained by multiplying the water vapor budget equation from Zhang et al. (2002) by the latent heat of vaporization:

$$\frac{d}{dt}(LE) = -\rho L_v (Q_{con} - Q_{ev}) + LHF \tag{3.7}$$

Terms on the RHS of (3.7) represent a source (sink) of LE due to evaporation (condensation) and the source of vapor via latent heat flux from the ocean/land surface. For the sake of energy conversion analysis, we have assumed here that $\rho L_v (Q_{con} - Q_{ev})$ can again be approximated by the heating rate. This approximation introduces errors because, by definition, the heating rate includes processes unrelated to LE, such as radiation and melting. However, we assume, as found in Zhang et al. (2002), that water vapor phase change processes (e.g. condensation, sublimation) dominate the heating rate.

The sum of (3.1), (3.6), and (3.7) yields, with significant cancellation of conversion terms, a total energy equation:

$$\frac{d}{dt}(TE) = -\nabla \bullet (p\vec{V}) - \vec{V} \bullet \vec{F} + LHF + SHF \tag{3.8}$$

Terms the RHS of (3.8) are the flux convergence of pressure, a loss of total energy due to dissipation of KE, and sources of latent and sensible energy due to fluxes at the ocean surface. In theory, the loss of KE due to internal friction is compensated by an increase in IE at the sub-grid scale, but this dissipative heating effect is not included in the model (Zhang and Altshuler 1999). Thus, friction represents a sink of total energy. The budget of total energy will not be discussed herein.

The intensification and maintenance of a tropical cyclone can be described as a series of energy conversions that take place within the secondary circulation. As moist air is drawn upward from the low-troposphere into the mid-troposphere and condensed into liquid water, LE is converted to TPE through condensation, C(LE,TPE). Mid-tropospheric warming causes a decrease in pressure at the ocean surface, which leads to an increase in the pressure gradient. As a result, the KE must increase, at the expense of TPE via adiabatic processes, in order to regain gradient balance. Thus KE is produced through a conversion from TPE, C(TPE,KE).

In short, moist convection converts LE to TPE. Some of the TPE is then converted to KE. TPE is the intermediary between two key components of TC energetics, KE and LE, whose characteristics and relationship will be expounded upon in the next section. Two specific conversions will be the focus of section 5:

$$C(LE,TPE) = \rho L_v (Q_{con} - Q_{ev}) \tag{3.9}$$

$$C(TPE,KE) = -\vec{V}_H \bullet \nabla p' \tag{3.10}$$

where C(A,B) represents a conversion from energy A to energy B. (3.9) is latent heat release (LHR) and (3.10) is the production of KE. The conversions can be expressed in reverse order simply by changing the sign on the right hand side of the equations.

4. System-Integrated Energetics

For the series of analyses to follow, we utilize the finest mesh, 4 km resolution data from the ZZW simulation. The finest mesh is activated at hour 12 of the integration and subsequently moved with the center of the storm every 6 hours. At each 15-min time interval within the 36-96 h time frame, we delineate a cylindrical volume of R = 200 km and z = 15 km, centered at the minimum surface pressure. As the storm moves, so moves the volume of integration. In this section, we present a time series of the left hand side (LHS) of (3.1) and (3.7), the total KE and LE, respectively, which are integrated within the R = 200 km domain. The 3D structure of KE at two times of interest is also discussed. Finally, we discuss the system-integrated KE and LE budget terms, the right hand side (RHS) of (3.1) and (3.7), that contribute to the energy evolution.

Fig. 3a shows that the amount of KE (RHS ordinate) is almost two orders of magnitude smaller than LE (LHS ordinate). On average, KE increases over time, except during 66 – 78 h. ZZW noted that both the simulated and observed Bonnie underwent a period of weakening during this period. After reaching peak KE at 65 h (Fig. 3c), the storm begins a partial eyewall replacement cycle, which is characterized by weakening of eyewall (in this case a partial eyewall) convection and subsequent reintensification. The KE during 65 – 96 h captures both of these stages. Specifically, the partial eyewall weakens rapidly (Fig. 2, 3b) after hour 65 and is eventually replaced by a full eyewall. Once the transition is complete, the axisymmetric eyewall intensifies in concert with the system-integrated KE. Changes in vertical wind shear are responsible for this structural transition (ZZW). For the period of interest in this study, hours 36-96, the total KE within the domain (R = 200km) increases by over 100%.

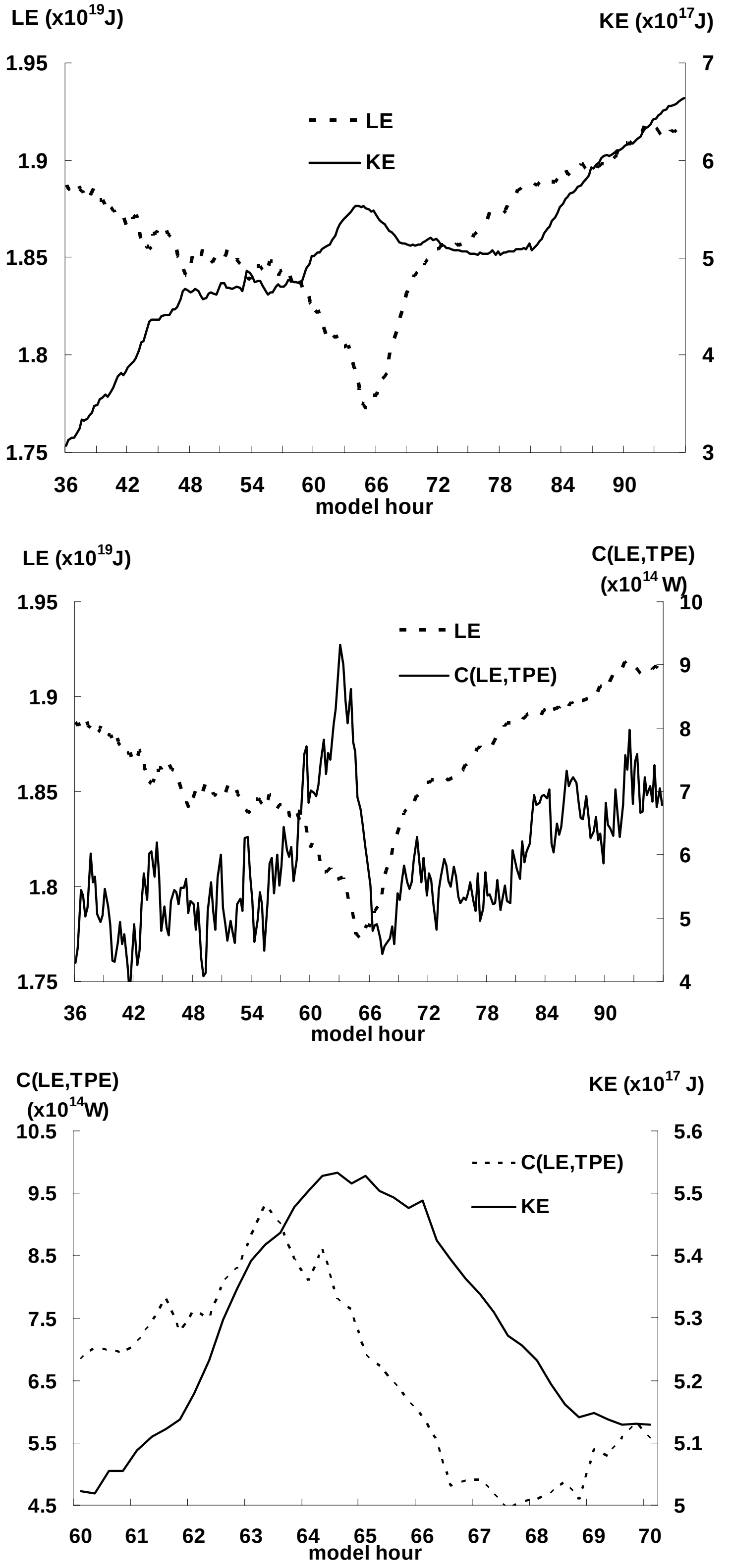

Figure 3: Time series (15 min) of the integrated LE and (a) KE and (b) C(LE,TPE) for a cylindrical volume with R = 200 km and Z = 15 km. The volume of integration is moved with the storm every 15 min. In (c), KE and C(LE,TPE) are plotted within the 60-70 h period.

The trend in LE (Fig. 3a) is much less drastic in magnitude than that of KE. The maximum variation of LE throughout the integration is only about 5%. The LE decreases during the first half of the integration, presumably due to rapid consumption of water vapor by latent heat release in the intensifying eyewall convection. At hour 65, however, there is an immediate shift to a positive trend of LE that persists through hour 96. The shift is coincident with the beginning of the eyewall replacement cycle (i.e. a similarly dramatic decrease in the magnitude of latent heat release, shown in Fig. 3b and 3c). Interestingly, at 63 h when the system-integrated latent heat release is maximum, the fraction of the eyewall that is filled with intense convection is very small (Fig. 2). Also of note is the lag of about 1.5 h between the peak of latent heat release and the peak of KE (Fig. 3c). Next, we discuss these changes by analyzing the 3D structure and budget of KE and LE.

At hour 47, the KE exhibits asymmetric structure along the west-east cross section (Fig. 4a). Vertical shear confines significant convection (dBz > 25) almost exclusively to the northeast semicircle of the storm (Figs. 4a, 5) and tilts the vortex downshear (Fig. 4a). At $z = 3$ km, the maximum KE is located in the eastern half of the eyewall (Fig. 5b), while at $z = 1$ km the maximum KE is confined to the northern half of the eyewall (Fig. 5a).

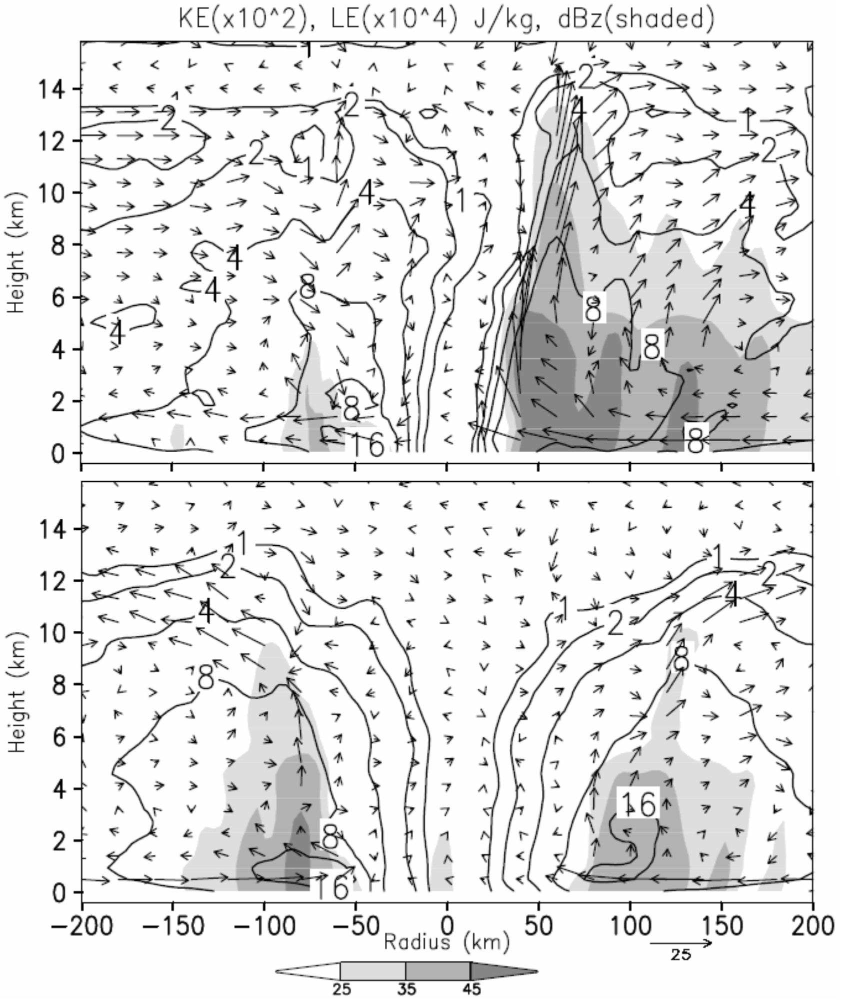

Figure 4: West-east vertical cross section through the center of Bonnie averaged during the (a) 46-47 h and (b) 96-97 h simulation. The solid contours are KE at intervals of 1, 2, 4, 8, and 16 (x10-2 Jkg-1. Superposed are the in-plane flow vectors. Radar reflectivity is shaded according to the color bar.

At hour 96, the KE structure and radar reflectivity are nearly symmetric in the vertical (Fig. 4b) and horizontal (Fig. 6a, 6b), consistent with the development of a full eyewall (Fig. 2). This transition occurs as the storm moves from a highly sheared environment to a weakly sheared environment between hours 48 and 96.

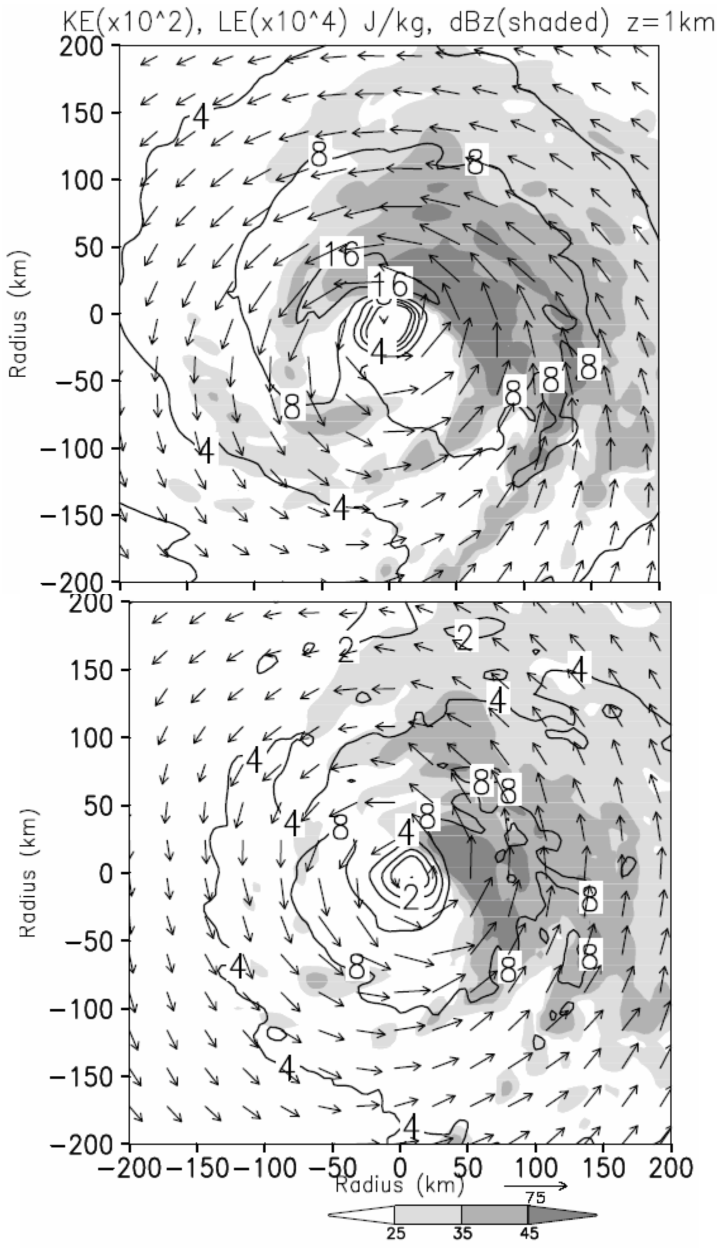

Figure 5: Horizontal cross sections of KE and radar reflectivity at (a) z = 1 km, (b) z = 3 km, taken as the average of the 46-47 h simulation. KE is contoured at intervals of 5e2 Jkg-1, and radar reflectivity is shaded according to the color bar. Horizontal flow vectors have been superposed.

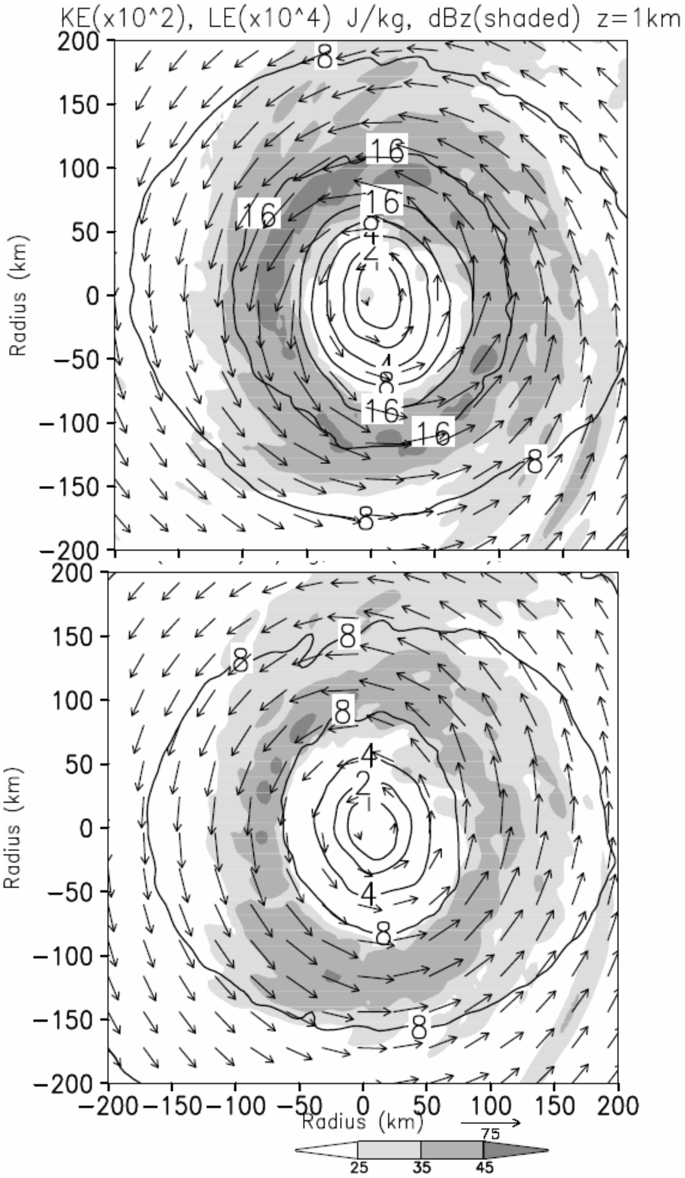

Figure 6: Horizontal cross sections of KE structure and radar reflectivity at (a) z = 1 km, (b) z = 3 km, taken as the average of the 96-97 h simulation. KE is contoured at intervals of 5e2 Jkg-1, and radar reflectivity is shaded according to the color bar. Horizontal flow vectors have been superposed.

The system-integrated KE budget is shown at 15-min intervals in Fig. 7a. The total change in KE is calculated (Eqn. 3.1) independently using both the sum of the budget terms (RHS) and directly from the trend in Fig. 3 (LHS at hourly intervals). The dominant energy balance is between friction (DISS) and KE production (C(TPE,KE)). Since the coordinates of our calculations follow the movement of the storm, all of the budgets must include the fluxes of energy from the lateral boundaries (BFLX), and the contribution of this flux is non-negligible.

During the 36-63 h time frame, the budget terms generally increase in magnitude (Fig. 7a), as expected for an intensifying storm where increasing KE production should be balanced by increasing friction. The KE production is highly variable during the 42 – 60 h period and is responsible for the high-frequency variations of KE during this period (Fig. 3a). The evolution of friction is smoother than the KE production, since friction is related more closely to the primary circulation, while KE production is related to the secondary circulation near the core of the storm. The integrated KE production is positive in the boundary layer and negative above the boundary layer (Fig. 7c), with the net production positive. The KE production and friction are negatively correlated and in approximate balance, and the lateral boundary flux (BFLX) imports the difference.

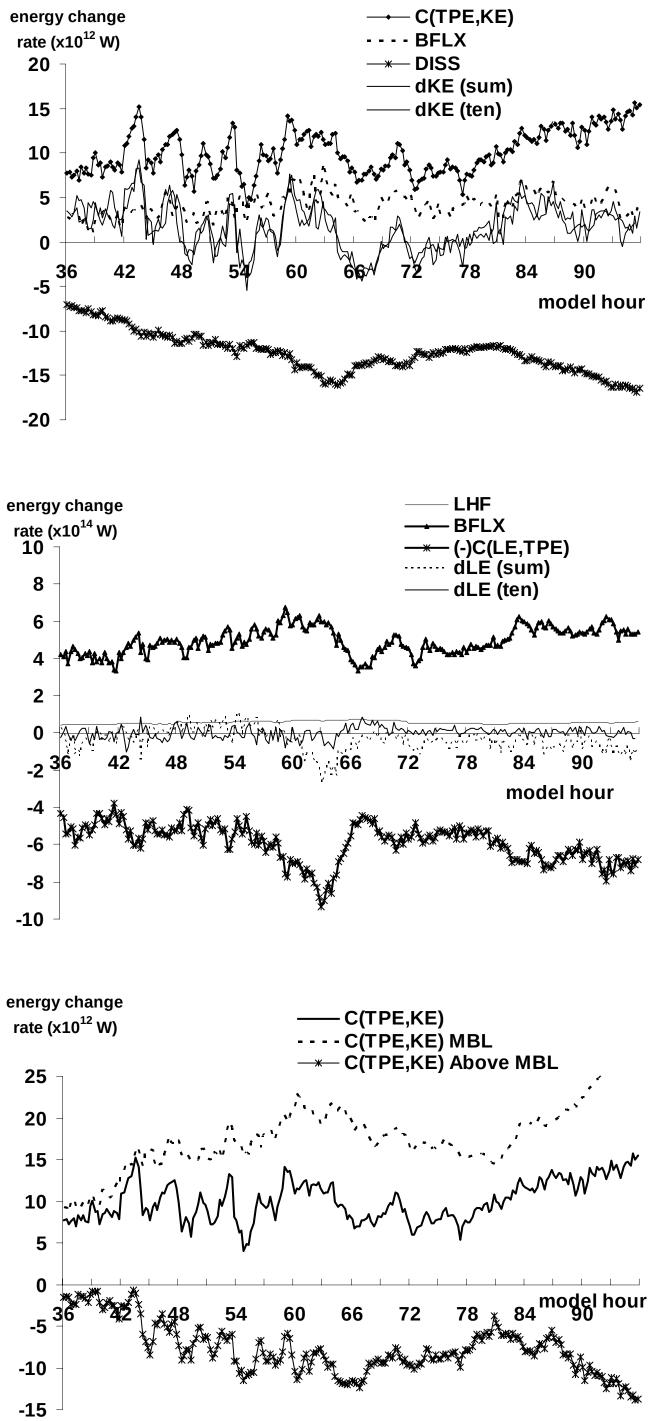

Figure 7: Time series (15 min) of the integrated (a) KE and (b) LE budgets for a cylindrical volume with R = 200 km and Z = 15 km. The volume of integration is moved with the storm every 15 min. In (c) C(TPE,KE) is shown as a total and in components within the boundary layer (MBL, dashed) and above the boundary layer (Above MBL, marked line).

At 60 h the KE production begins to decrease, but the friction does not begin to decrease in magnitude until 63 h. Thus, the frictional sink of KE is temporarily greater than the other source terms. This leads to a decrease in KE until the KE production and boundary flux increase again, consistent with the eyewall replacement cycle. Friction lags KE production because the radial production of KE is not instantly assimilated into the azimuthal flow. In general, the budget captures very well the evolution of KE.

The total change in LE (Fig. 7b) is also calculated independently (using the LHS and RHS of Eqn. 3.7) in the same way as the KE budget. The dominant energy balance is between the loss of LE to condensation and the import of LE into the domain through the lateral boundaries. LHF from the ocean surface contributes a small amount of LE, but considering the small magnitude of the LE change, the ocean source is crucial to the maintenance of energy balance.

To understand this dramatic shift in LE tendency from negative to positive that occurs at hour 65 (Fig. 3a), we look at the individual LE budget terms (Fig. 7b). For the majority of the 36-96 hour integration, the sink of LE due to condensation is nearly equal, almost a mirror image in the budget time series, to the flux from the lateral boundaries. Any consumption of LE by convection is replaced primarily by lateral import (BFLX) and secondarily by the ocean flux (LHF). The negative LE tendency from 36 – 65 h is attributable to the fact that the storm consumes slightly more LE than is replaced. However, one anomaly in the mirror image occurs around 63 h. At this time convection rapidly increases, but the lateral boundary flux of LE does not correspondingly increase. This may be due to the fact that at 63 h, the area of the eyewall that is filled with convection (Fig. 2) is extremely limited. Thus the area from which the storm can draw more LE is similarly limited. Without sufficient BFLX of LE to support intense convection, the eyewall convection rapidly decays, marking the beginning of the eyewall replacement cycle. After 66 h, Bonnie regains its intensity as both LHR and BFLX increase in magnitude. The LE tendency remains positive but decreases in magnitude (Fig. 3).

Although LE and KE are related, only a very small amount of TPE produced through (3.9) is actually reconverted to KE via (3.10). Fig. 8a compares the conversion terms in (3.9) and (3.10). The KE production is about one order of magnitude smaller than the LHR, but their evolution is positively correlated. This implies that if more LE is converted to TPE, then more KE would be produced from TPE. Fig. 8b, however, shows that the ratio of C(LE,TPE) to C(TPE, KE) is not constant in time. In fact, this measure of efficiency of energy conversion varies within 1%-2.5%. Of interest is that the efficiency of KE production is positively correlated with the relative axisymmetry of the storm, as seen by comparing Fig. 2 and Fig. 8c. During 42 - 63 h, convection is increasingly concentrated into a smaller and smaller fraction of the eyewall (Fig. 2), and this corresponds to decreasing efficiency (Fig. 8b). Then after 63 h, when Bonnie begins the process of axisymmetrization, efficiency increases as the fraction of the eyewall that is convection-filled increases. In Fig. 8c, it can be seen that while the C(LE,TPE) increases rapidly from 54 – 63 h, the number of points with significant updraft speeds actually decreases when it would be expected to increase significantly. This confirms that the convection, while extremely intense, is being concentrated into a very small fraction of the eyewall. It is possible that while an asymmetric hurricane can intensify, as Bonnie did under the influence of vertical wind shear, the energy conversions that lead to a high-KE TC are more efficient in storms with an axisymmetric structure. The next section will address the 3D structure of these two key conversion terms.

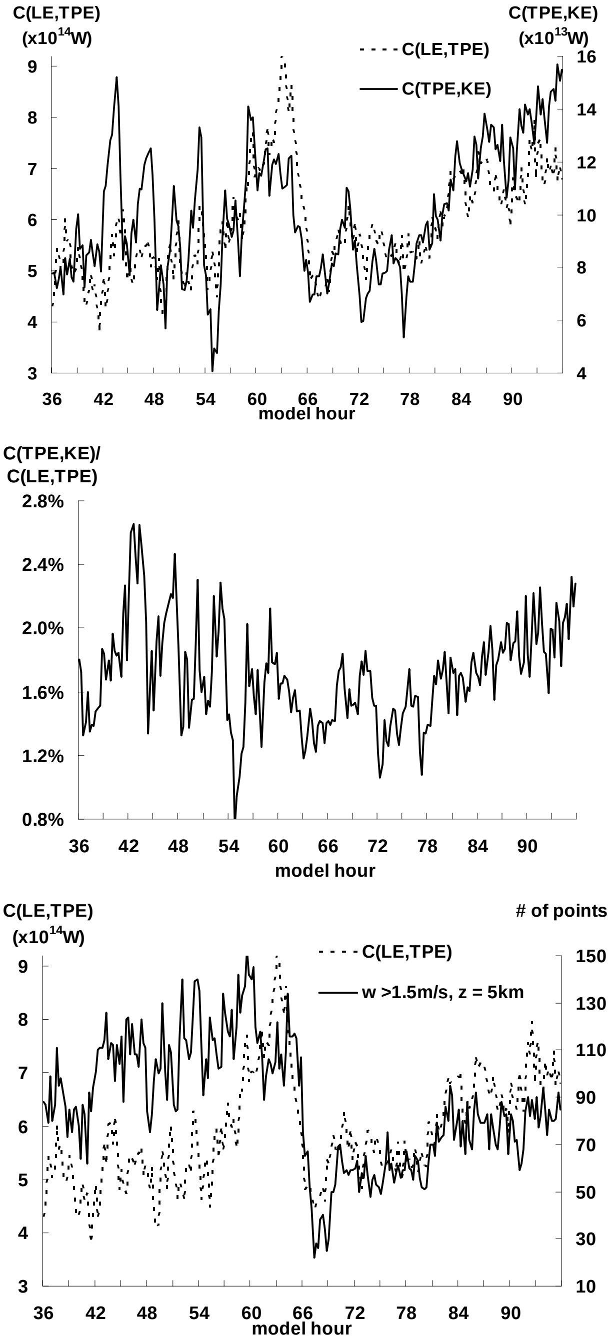

Figure 8: As in Fig. 7, but a) isolating the two predominant conversion terms, C(LE, TPE) (dashed, left axis) and C(TPE, KE) (solid, right axis), (b) comparing the C(LE,TPE) (dashed, left axis) and the number of gridpoints characterized by an updraft greater than 1.5 ms-1 at z = 5 km (solid, right axis), and (c) the ratio of the two conversions in (a).

5. Structure of Energy Conversions

The two structural phases (partial and full eyewall) and the transition between them can be seen in the time evolution of radar reflectivity (Fig. 2). In this section we present the structure of characteristic energy conversions associated with the two characteristic phases.

At hour 47, the most significant energy conversions occur in the northeast quadrant of the storm. Here, the KE production (Fig. 9a) exhibits a cohesive structure. In the boundary layer (Figs. 9a, 10a), inflow up the pressure gradient produces large amounts of KE. The outward tilt of the eyewall with height facilitates consumption of KE (Figs. 9a, 10b) above the boundary layer as the updraft flows slightly down the pressure gradient. The KE production is very large and positive in the boundary layer, and small and negative above the boundary layer (Fig. 7c). In the western half of the storm, the production in the boundary layer is minimal, and the return outflow (Figs. 9a, 10a) consumes KE. The upper level inflow toward the center of the storm (i.e. up the pressure gradient), though small, is a source of KE (Figs. 9a, 10b).

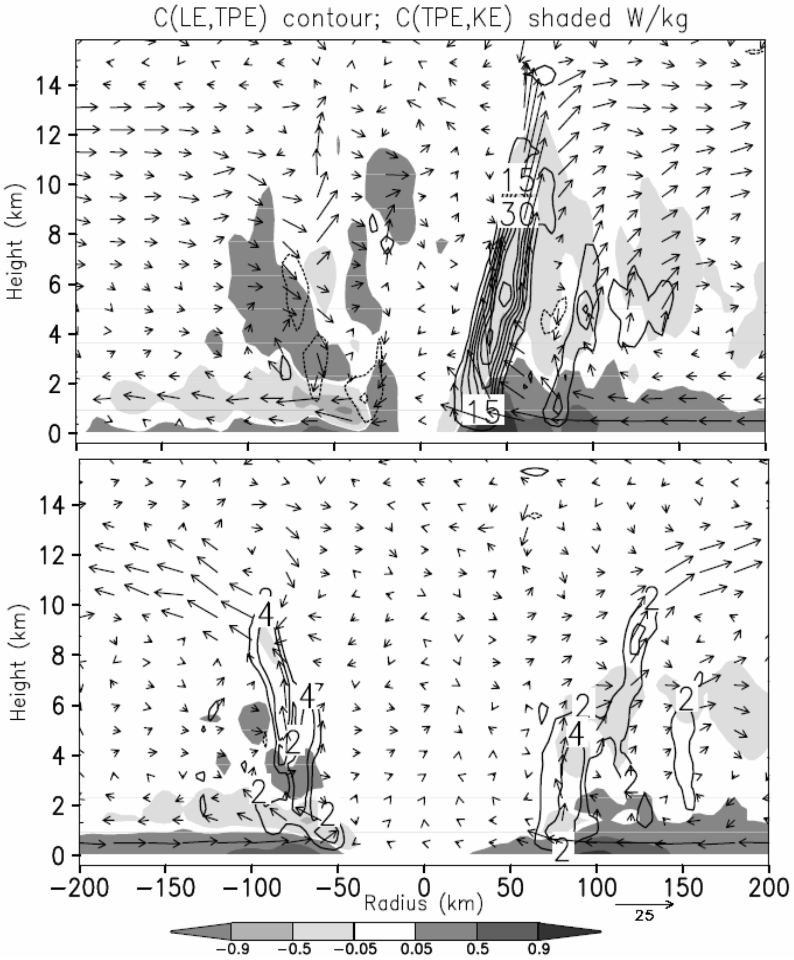

Figure 9: West-east vertical cross section through the center of Bonnie of energy conversion terms, averaged during the (a) 46-47 h and (b) 96-97 h simulation. The C(LE,TPE) is contoured in (a) at intervals of 5 Wkg-1 and in (b) at -2, 2, 4, and 8 Wkg-1, and C(TPE, KE) is shaded in both (a) and (b) according to the color bar. Superposed are the in-plane flow vectors.

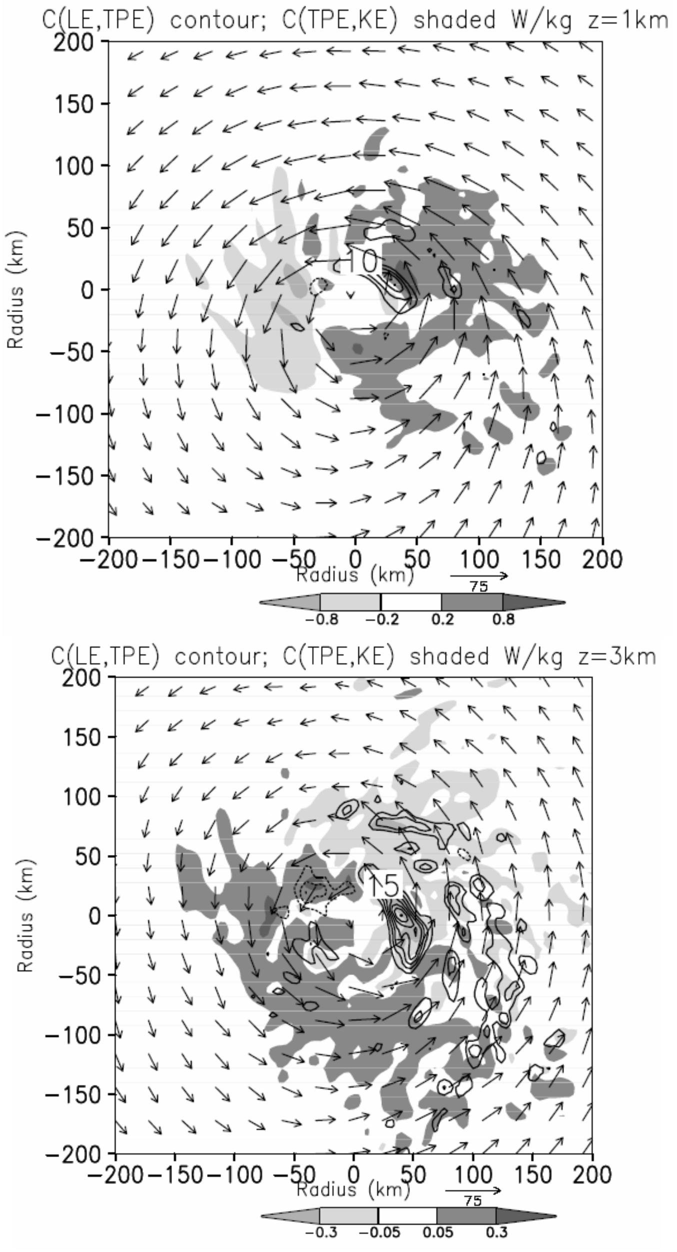

Figure 10: **Horizontal cross sections at 46-47 h for C(LE,TPE), contoured, and C(TPE,KE), shaded according to the color bar, taken at (a) z = 1 km and (b) z = 3 km. In-plane flow vectors have been superposed. C(LE, TPE) in (a) is contoured at intervals of 3 Wkg-1, and in (b) is contoured at intervals of 5 Wkg-1.**

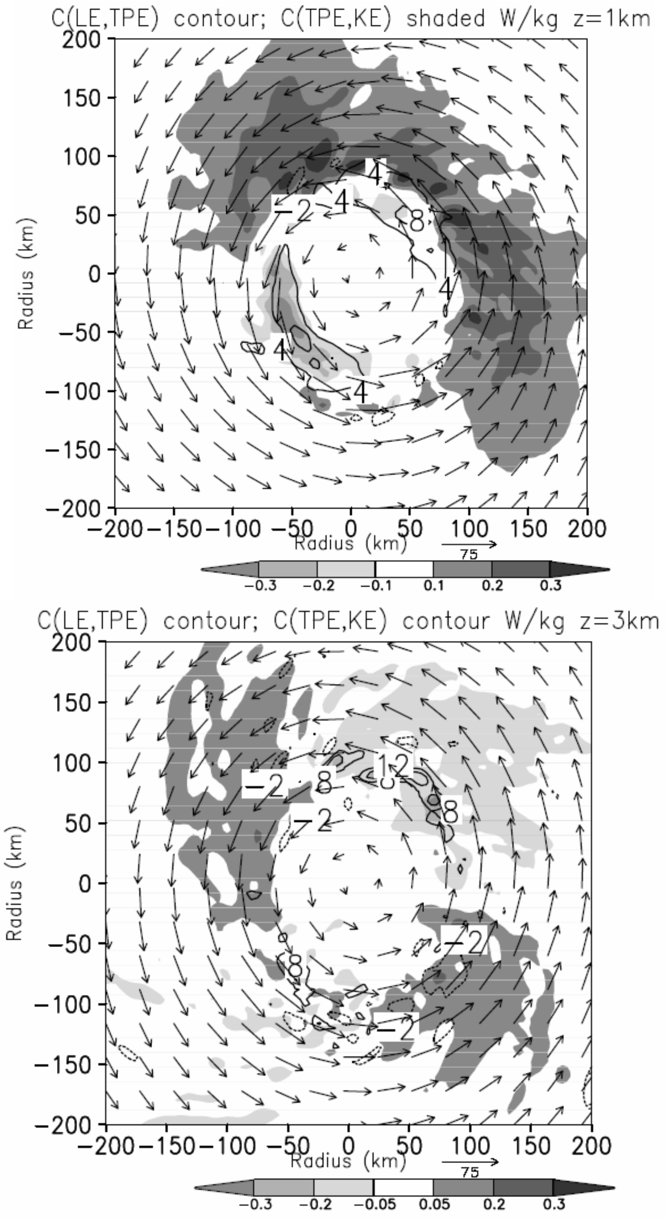

Figure 11: Horizontal cross sections at 96-97 h for C(LE,TPE), contoured, and C(TPE,KE), shaded according to the color bar, taken at (a) z = 1 km and (b) z = 3 km. Horizontal flow vectors have been superposed. C(LE,TPE) is contoured at intervals of -2, 2, 5, 8, and 11 Wkg-1 in (a) and intervals of 5 Wkg-1 in (b).

As shown in the previous section, the LHR is coupled very closely with the KE production (Figs. 9 and 10). In the eastern half, LHR in the convective towers of the main eyewall (R = 50 km) and the secondary eyewall (R = 100km) represents a strong source of TPE, some of which is converted to KE in the boundary layer, directly below the location of maximum latent heat release (Figs. 9a and 10b). In the western half, however, almost no convective activity is ongoing, so there is no conversion of LE to TPE, and hence, very little KE production at the surface. In fact, a negative LHR (Figs. 9a and 10) exists in the western "eyewall," probably due to subsidence drying and evaporation of cloud elements that have been advected cyclonically from the eastern half.

By hour 96, Bonnie exhibits nearly axisymmetric structure. In the boundary layer, KE is being produced (Figs. 10b and 11a) throughout most of the azimuthal extent of the storm. The maximum value of KE production at 96 h is significantly less than that at 47 h, consistent with the assertion that the vertical wind shear at 47 h suppresses the western convection and enhances the eastern convection.

In the eyewall at 96 h, KE consumption occurs in the outward slanting updrafts of each half, less so in the western half where the low level return outflow is responsible for consuming some KE. The consumption is much less than the production, consistent with a storm of increasing intensity (Figs. 3 and 7b). The maximum magnitude of LHR at 96 h is significantly less than that in the eastern half at 47 h (Fig. 9a), but it covers a much greater azimuthal extent (Fig. 11).

6. Mean and Eddy KE

Since the structure of Bonnie varied from highly asymmetric to axisymmetric during the lifetime of the storm, it is useful to analyze the processes by which this structural transition occurred. We will present the eddy KE budget and the structure of important processes that facilitate the generation and decay of asymmetries.

In this section we present the equations for mean and eddy KE in cylindrical coordinates. The full derivation is presented in the appendix. For the purposes of this study, total KE is defined at each grid point as

$KE = \overline{K} + K'$, where $\overline{K} = \frac{1}{2}(U^2 + V^2)$ and $K' = \frac{1}{2}(\overline{u'^2} + \overline{v'^2})$,

where $\overline{K}$ is the azimuthal mean of KE, and K' is the azimuthal mean of the deviation from $\overline{K}$. U (V) and u' (v') are the azimuthal mean and the deviation from the mean of the radial (azimuthal) wind. The overbar denotes azimuthal average.

TK75 noted that the mean and eddy flows are highly dependent on how the mean is defined. The definition of the mean naturally depends on the definition of the storm center, around which the azimuthal average is calculated. Unlike many previous energy studies that did not include environmental flow (e.g., TK75 and Wang 2002), the asymmetries of Bonnie are directly influenced by vertical shear, which introduces difficulties.

The effects of the wind shear are two-fold. While shear does generate the real asymmetries in the storm, it also tilts the central axis of the vortex downshear (Fig. 4a), especially in the upper troposphere. This vortex tilting introduces nonphysical asymmetries when azimuthal averaging is conducted around an upright central axis. To deal with this problem, we have chosen to calculate the center using the minimum pressure of the vortex at each vertical level up to 12 km. The minimum pressure is not necessarily the geometric center of the vortex, but it is assumed so for this study. Then, prior to azimuthal averaging we restack the vortex into an upright position. This creates a discontinuity in vertical velocity, and for this reason, the equations are derived (see appendix) in such a way that there are no vertical derivatives. This allows the quantities to be calculated in a physically realistic manner without introducing artificial asymmetries due to tilting.

The equation for $\overline{K}$ can be represented as

$$\frac{d\overline{K}}{dt} = -BTC + PTM + DISM \quad , \qquad (6.1)$$

where BTC is the barotropic conversion of energy between the mean and the eddy vortex. PTM represents the conversion of mean PE to K, and DISM is the dissipation of $\overline{K}$ due to frictional processes, including horizontal and vertical diffusion. See Appendix.

The equation for K’ can be represented as

$$\frac{dK'}{dt} = BTC + PTE + DISE \quad , \qquad (6.2)$$

where BTC is identical, but with an opposite sign, to the term in (6.1), PTE is the conversion of eddy PE to K’, and DISE is the dissipation of K’ due to frictional processes.

In this section, we first address the evolution of volume-integrated KE, K, and K’. Then, the volume-integrated budget for K’ is analyzed in a similar fashion to that of the total KE in Section 4. Then we analyze the 3D structure of both $\overline{K}$ and K’, as well as notable budget terms for K’.

Fig. 12a shows the domain-integrated time series of KE, K, and K’ throughout the 36 - 96 h period of the integration. The evolution of $\overline{K}$ resembles very closely that of KE, since the majority of KE is contained within the mean vortex. K’, the difference between KE and $\overline{K}$, is an order of magnitude smaller than $\overline{K}$ and is characterized by growth and maintenance prior to 65 h and decay until 78 h, after which K’ remains constant and very small.

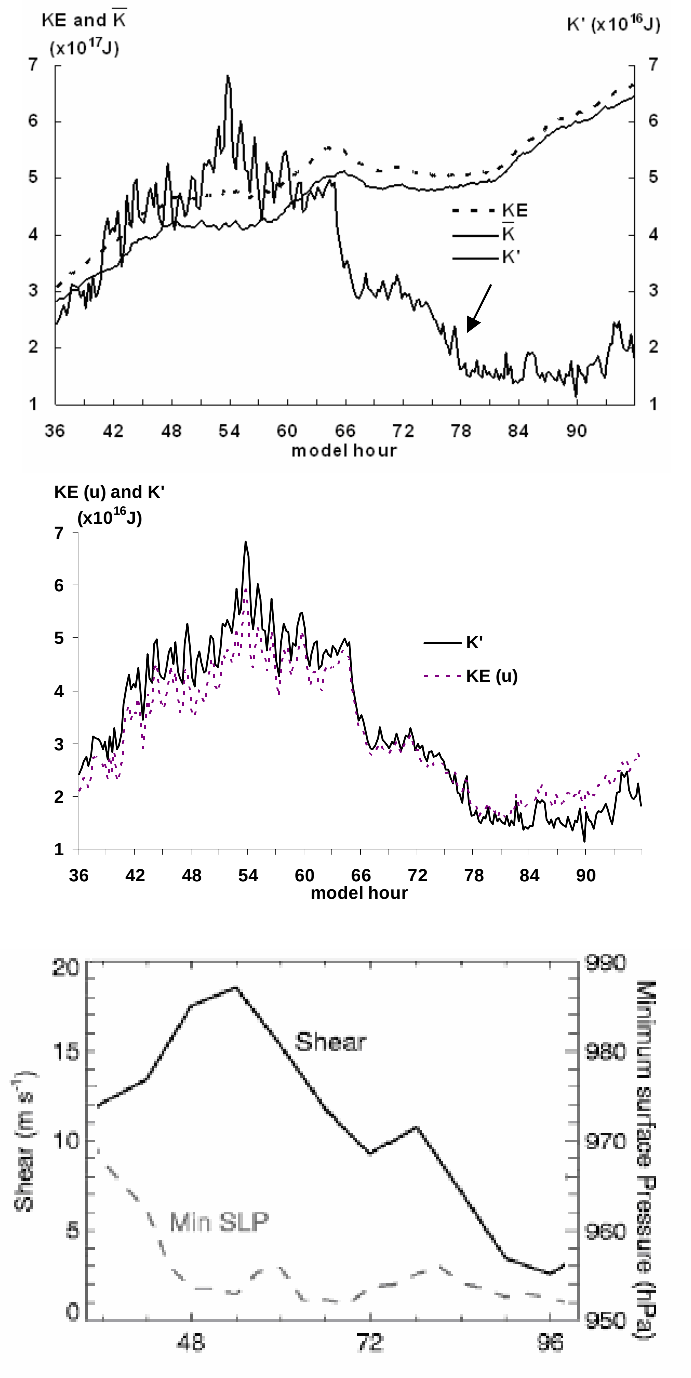

Figure 12: (a) Time series (15 min) of the volume-integrated KE (solid, left axis), $\overline{K}$ (dashed, left axis) and K’ (solid, right axis) for a cylindrical volume with R = 200 km and Z = 15 km. (b) Time series comparing $\overline{K}$ and K’ with the KE decomposed into U (dashed, right axis) and V (dashed, left axis). The volume of integration is moved with the storm every 15 min. (c) Time series of area-averaged vertical shear and minimum sea level pressure, from Zhu et al. (2004).

Superimposed on the K' growth and decay are high-frequency fluctuations that are associated with conversions between $\overline{K}$ and K' that occur primarily from 42 – 65 h. The fluctuations have a period of about an hour. At 40 h and 65 h, K' jumps drastically, increasing and decreasing in magnitude by about half in the span of about an hour.

The evolution of K' in Bonnie follows closely the evolution of vertical wind shear (see ZZW's Fig. 9a, Fig. 12c herein), which increases until 54h and then decreases until after 96h. Since the vertical wind shear drives the development of asymmetric diabatic heating, and diabatic heating is the ultimate source of KE, it can be concluded that *vertical wind shear is the dominant factor leading to the development of K' in Bonnie*. In fact, the drastic jumps in K' around 42 h and 65 h occur at the same time as similarly rapid changes in LHR (Fig. 3b), and also at vertical wind shear of about 13 m/s. Also, almost all of the K' variability can be accounted for in the radial KE (Fig. 12b), so the effect of vertical shear in the case of Bonnie was to disrupt the secondary circulation, but not the primary, azimuthal circulation.

The evolution of the mean and eddy vortex can be separated into two periods. The 42 - 65 h period can be characterized by K' growth and maintenance with large, high-frequency fluctuations with a period of about an hour. The 65 - 96 h period can be characterized by K' decay with smaller magnitude fluctuations. High-frequency fluctuations in the growth rate are related to the relationship of $\overline{K}$ and K', i.e. BTC. After the bifurcation at 65 h, however, while K' is decaying, $\overline{K}$ undergoes a significant fluctuation related to the partial eyewall replacement cycle. Since K' is small during the fluctuation, it can be concluded that *the beginning of the eyewall replacement cycle at 65* *h marks the end of the shear-forced asymmetry regime and the beginning of the axisymmetric regime .*

The 3D structure of $\overline{K}$ and K’ can provide insight into regions of the storm where important processes are acting. In Fig. 13a, the 3 hourly data is not able to resolve the drastic jumps and high-frequency fluctuations, but it is used to show the general evolution of radially-averaged $\overline{K}$ and K’ throughout the lifetime of the storm. Prior to 42 h, asymmetries develop throughout the troposphere, but as the wind shear increases, asymmetries near the surface dominate after 42 h. After 65 h, K’ decays throughout the depth of the troposphere. This is an indication of the axisymmetrization process.

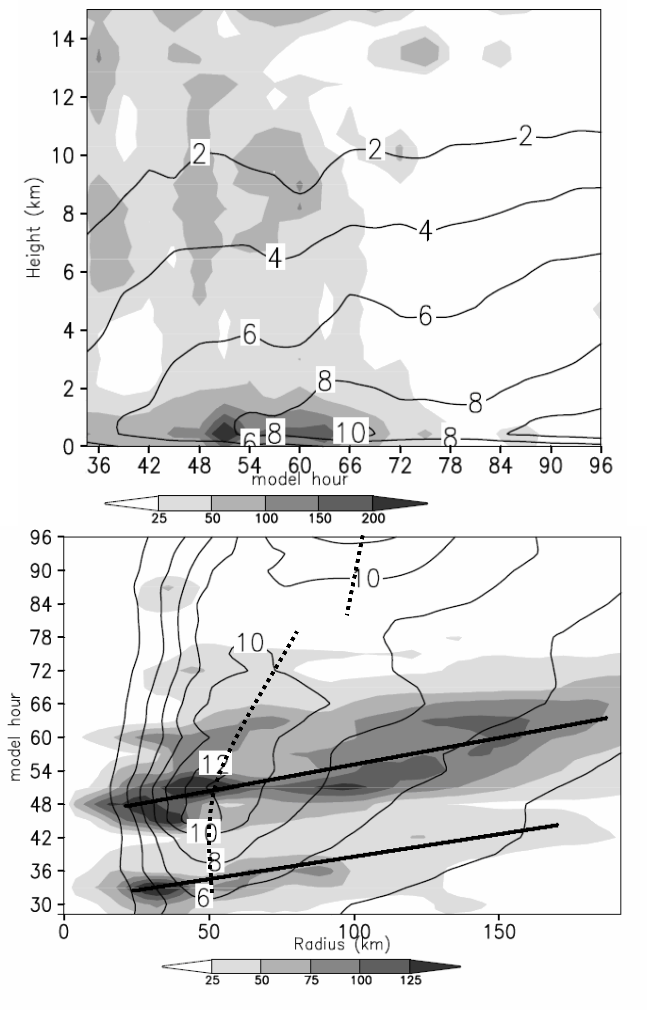

Figure 13: a) Time series of radially-averaged (r = 150 km) $\overline{K}$ (contoured at intervals of $1\text{x}10^2$ Jkg^{-1}) and K' (shaded), and b) time-radius cross section of vertically-averaged (below 5km) $\overline{K}$ (contoured at intervals of $1\text{x}10^2$ Jkg^{-1}) and K' (shaded). Heavy lines in b) denote the outward propagation of asymmetries, and dashed line denotes the RMK.

$\overline{K}$ (Fig. 13a) is confined primarily to the lower troposphere and increases until 65 h, when the eyewall replacement cycle begins. $\overline{K}$ in the lower troposphere decreases from 66 - 78 h, after which it begins to increase again until the end of the integration. This pattern is characteristic of the well-documented eyewall replacement cycle.

Because of the dominance of low-level asymmetries, only the lowest 5 km have been considered in the vertical averaging of Fig. 13b. It can be seen that K' develops first inside the radius of maximum $\overline{K}$ (RMK) and appears to propagate outward with time. The primary maxima in K' occurs in the 48 - 54 h period (Figs. 12a and 13). After 65 h, K' quickly dissipates, while $\overline{K}$ (Fig. 12b) shows evidence of the eyewall replacement process in the absence of significant K' processes.

Fig. 14 shows the vertical structure of $\overline{K}$ and K' at 47 h and 96 h, which are times characteristic of high and low asymmetry, respectively. At 47 h (Fig. 14a), significant asymmetries exist in the inflow and in the outflow. This indicates again that the primary asymmetries are associated with the radial, secondary circulation. Strong inflow, an intense and vertically erect updraft, and outflow at z = 13 km characterize the secondary circulation. The asymmetry near the RMK in the low levels (Fig. 14a) is the most significant and is a product of the asymmetric low-level inflow that causes the eye to take on non-circular characteristics.

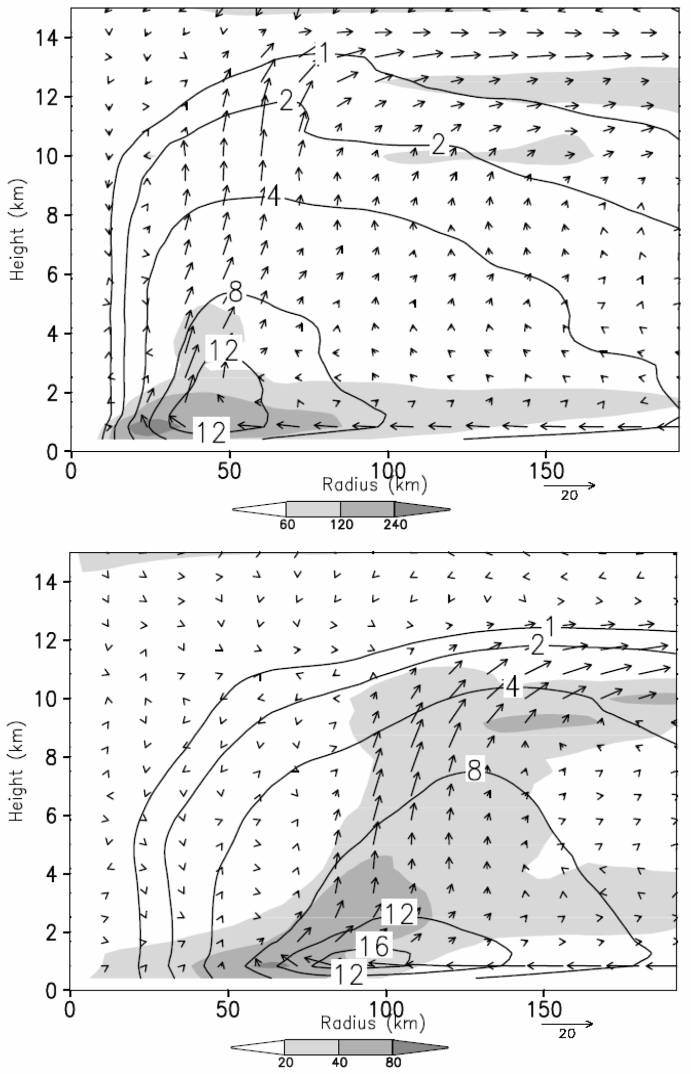

Figure 14: Height-radius cross sections of $\overline{K}$ (contoured at intervals of 1, 2, 4, 8, 13, and 16 x10^2 Jkg^{-1}) and K' (shaded) for (a) t = 46 - 47 h and (b) t = 95-96 h averages. K' is shaded according to the color bars. The azimuthally averaged in-plane flow vectors are superposed.

At 96 h (Fig. 14b) the values of $\overline{K}$ are larger than at 47 h, indicating a more powerful storm. The maximum K', however, is only a third of that at 47 h, though it occurs in the same location inside the RMK. Compared to 47 h, the low level inflow is stronger, the updraft is more outward-sloping, and the outflow occurs lower (z = 10-12 km). The small magnitude of K' at 96 h is a clear indication that the storm has escaped vertical shear and can be characterized as axisymmetric.

Fig. 15 clarifies the processes that dictate the evolution of K' throughout Bonnie's evolution. Eqn. 6.2 has been volume integrated. Before discussing the evolution of processes, it is important to discuss the weaknesses of the quasi-Lagrangian methodology used in this study. First, in the derivation, we assume that the storm is in hydrostatic balance. Also, $\overline{K}$ and K' are redefined for each 15 m calculation. This casts uncertainty on the previous 15 m prediction, which was made for what could be a significantly *different* mean and eddy vortex. Bearing these uncertainties in mind and understanding that a perfect budget is not possible, the methodology is able to capture the evolution of both $\overline{K}$ and K' quite well (Fig. 15).

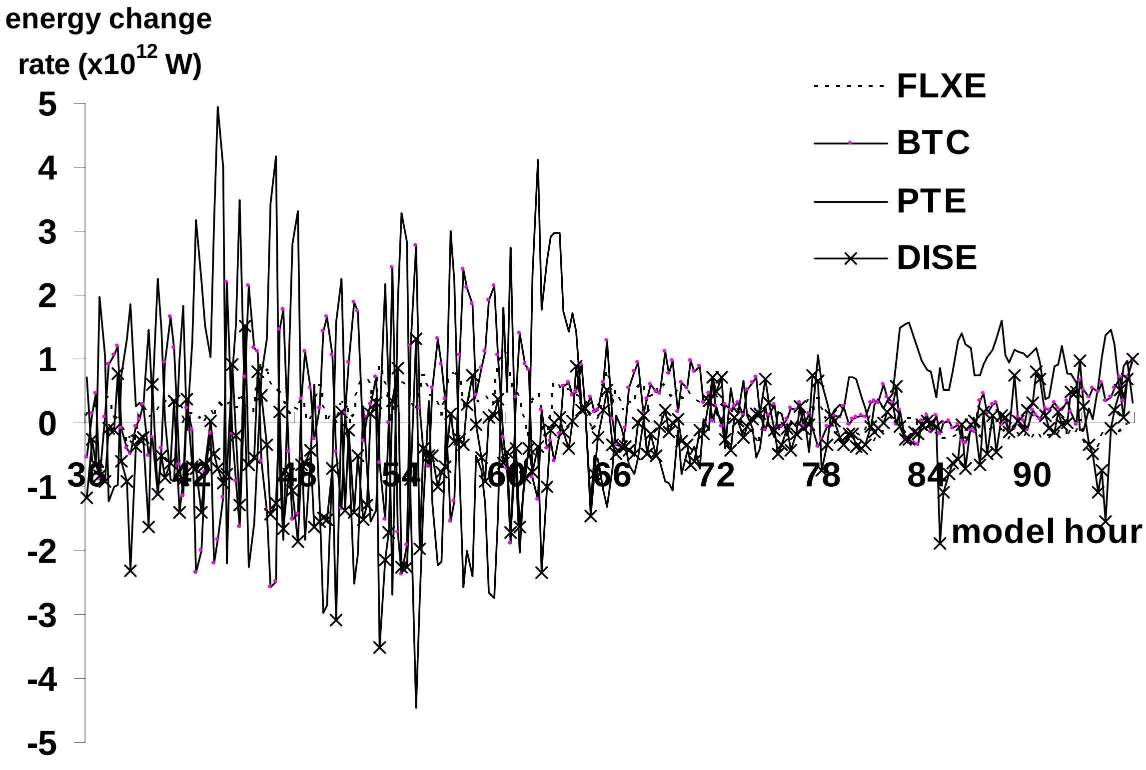

Figure 15: Time series (15 min) of the volume-integrated K' budget for a cylindrical volume with R = 200 km and Z = 15 km. The volume of integration is moved with the storm every 15 min.

The KE (Fig. 7a) and $\overline{K}$ (not shown) budgets expectedly appear almost identical. The only significant difference between the KE budget and the $\overline{K}$ budget is that the $\overline{K}$ budget includes the BTC term that represents conversion to K'. The primary balance of $\overline{K}$ is between PTM (or C(TPE, K)), DISM, and BFLX. The BFLX term appears when Eqn. 6.1 is volume integrated, and it imports $\overline{K}$ at all times. BTC will be discussed in the next section as part of the K' budget. The 3D structure of KE budget terms, which is very similar to those of K, has been well-covered in Sections 4 and 5, as well as in many other observational and modeling studies. We will not address it further.

The K' budget (Fig. 15) is considerably more complicated. Generally the storm imports K' (FLXE), friction (DISE) dissipates K', and BTC and PTE fluctuate and are negatively correlated. BTC and PTE are responsible for the high frequency fluctuations of K' in Fig. 12b. From Fig. 15, it can be seen that PTE is a source of K' when K' is growing, but it is a significant sink of K' when K' is decreasing. From our analysis, it appears that *PTE dictates the growth rate of K'*.

At 48 h, BTC and PTE are responsible for most of the K' production in the boundary layer (Figs. 16a, 16b) at all radii, and both BTC and PTE are sinks of K' in the eyewall above the boundary layer. The FLXE (Fig. 16c) term represents the advection of K' due to both the mean and eddy vortex, and it removes K', produced by BTC and PTE, from the boundary layer.

At 96 h, the magnitude of budget terms is nearly an order of magnitude smaller than at 48 h. Structure is similar to that found by Wang (2002), with PTE contributing the most to the development of K' (Fig. 17a). BTC is a source of K' in the boundary layer outside of the eyewall, and it is a sink of K’ inside the eyewall and in the eye. FLXE again removes K’ from the boundary layer.

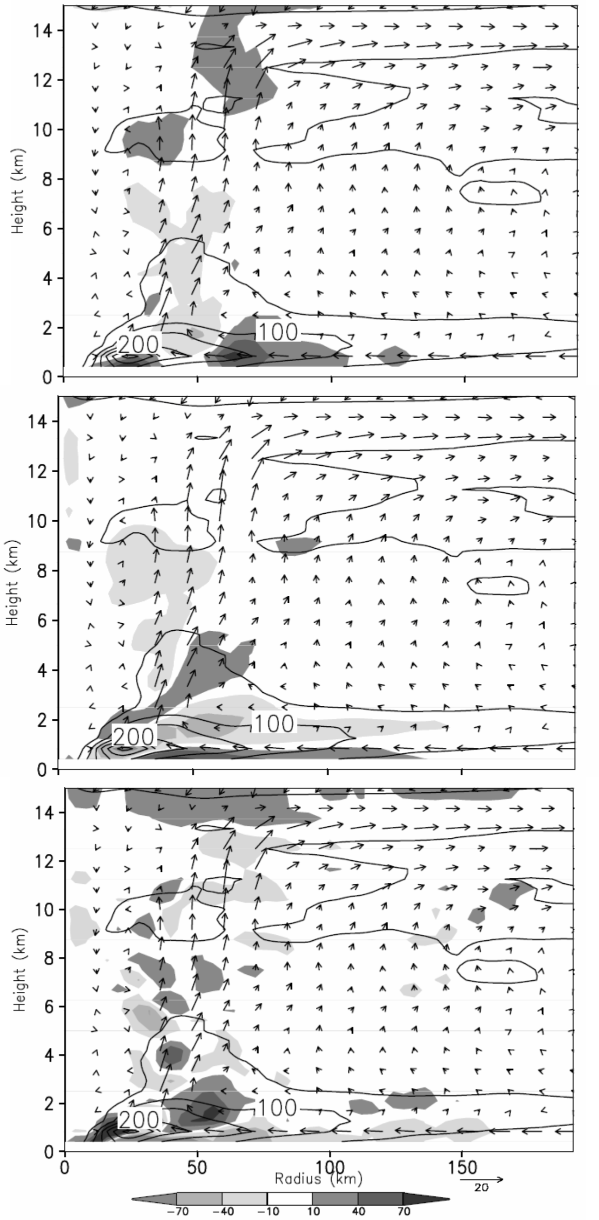

Figure 16: Height-radius cross sections of K’ contoured at intervals of 50 J/kg. Shaded are a) PTE, b) BTC, and c) FLXE shaded according to the color bar in units of 1x10-3 W/kg. In-plane flow vectors have been superposed, and quantities are hourly averages at 47-48 h.

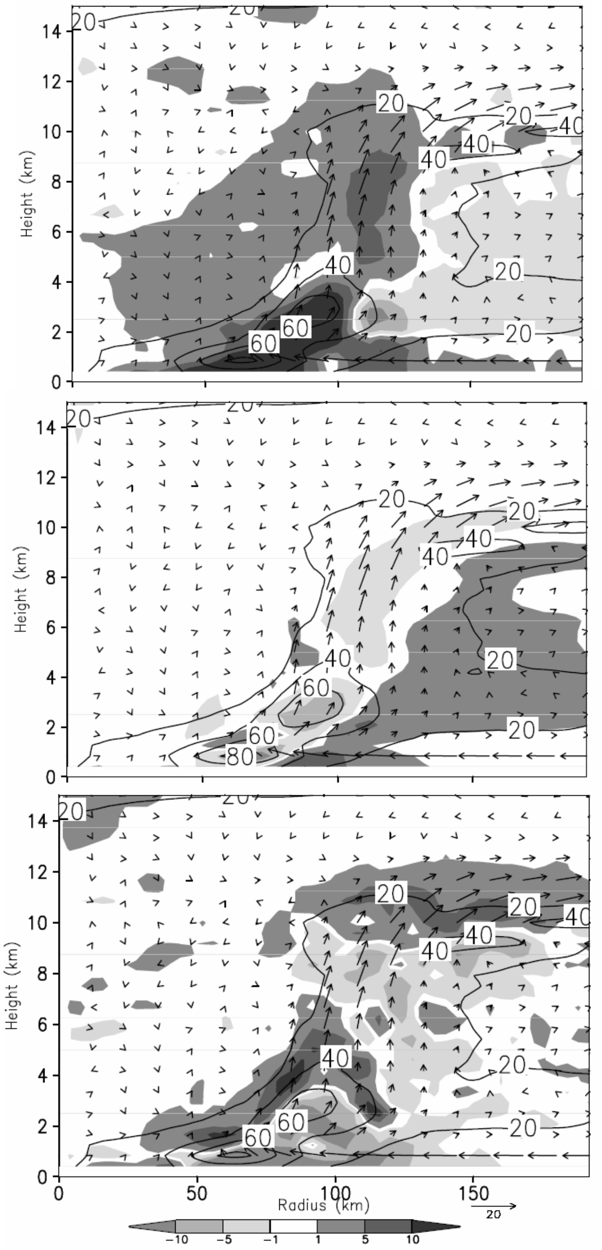

Figure 17: As in Fig. 16, with K' contoured at 20 J/kg and valid at 95-96 h.

The fluctuation of BTC and PTE is due to the episodic anomalous inward penetration of the radial wind (not shown). The inward penetration is caused by asymmetric diabatic heating and aids in breaking down the circularity of the eye. Fig. 18 shows how the radial and azimuthal wind fluctuates at the eye-eyewall interface during the shear-driven phase of the storm and the remains constant during the axisymmetric phase. This behavior is due to the influence of vertical shear, which acts to drive asymmetries only early in the storm.

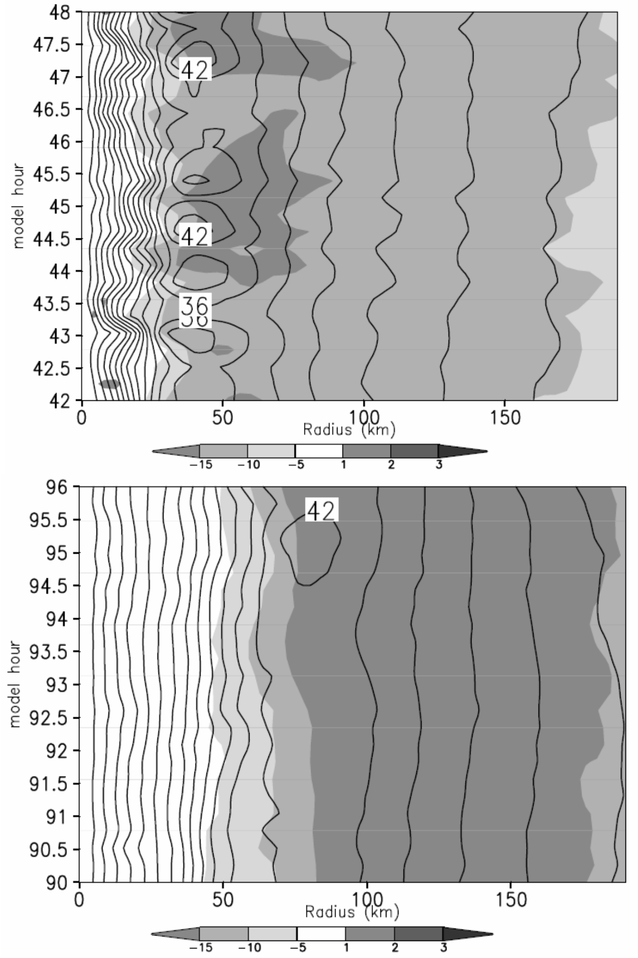

Figure 18: Time-radius cross section of V (contoured at intervals of 3 ms-1) and U (shaded) at z = 50m at a) 47-48h, and b) 95-96h.

Fig. 19 shows the horizontal structure of v' and K' (Fig. 19a) and u' and w' (Fig. 19b) during the asymmetric stage of Bonnie. The wavenumber-1 asymmetry can be seen in v' and K' at 47 h, with negative v' perturbations maximum in the southwest quadrant to the right of the shear vector and positive perturbations in the northeast quadrant associated with asymmetric convection. The asymmetric upward vertical motion associated with the convection can be seen (Fig. 19b) to occur also in the northeast quadrant, with the associated inflow located slightly downwind, owing to the strong cyclonic advection. This pattern of upwind tilt of wavenumber-1 asymmetries with height compares well to that found by Wang (2002, his Fig. 5) in an idealized study. At 96 h the structure of v’ (Fig. 20a) is similar in magnitude to that at 47 h, but the magnitudes of K’ (Fig. 20a), w’, and u’ (Fig. 20b) are much less, indicating the axisymmetrization of the storm.

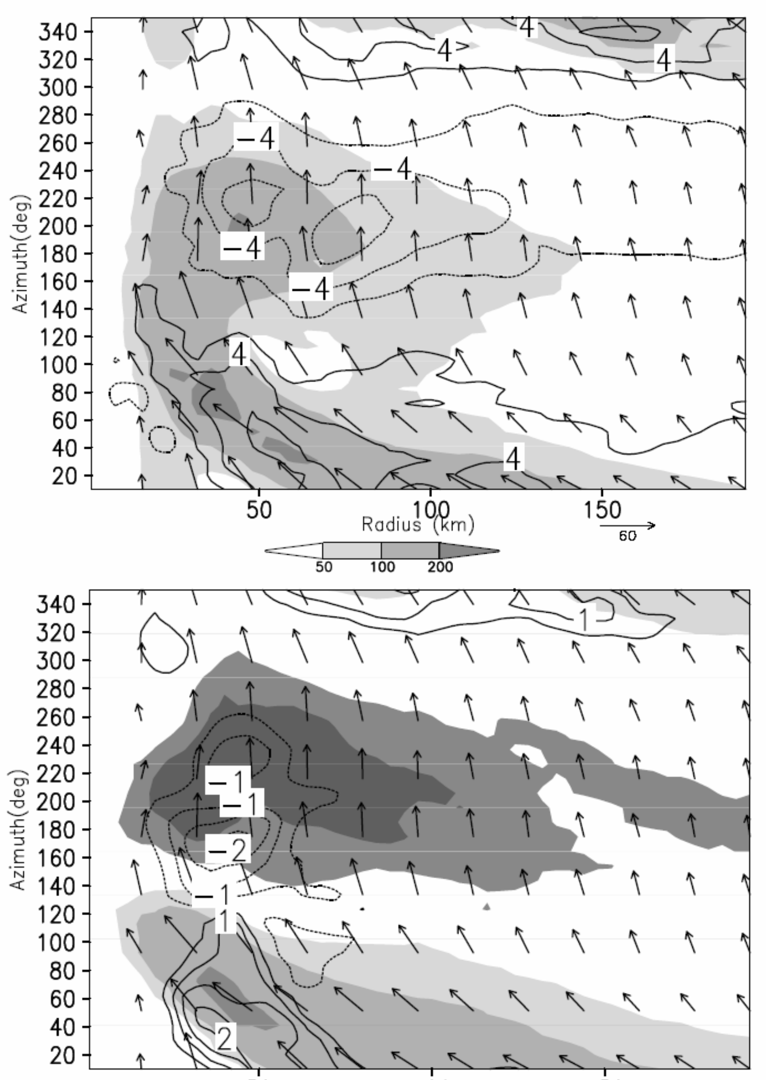

Figure 19: Azimuth-radius plot at 45-46 h of a) v’ (contoured at intervals of 2 ms-1) and K’ (shaded), both vertically averaged below z = 5 km, and b) w’ (vertically averaged from z = 1.5 to z = 10 km and contoured at intervals of 0.5 ms-1) and u’ (at z = 50 m, shaded).

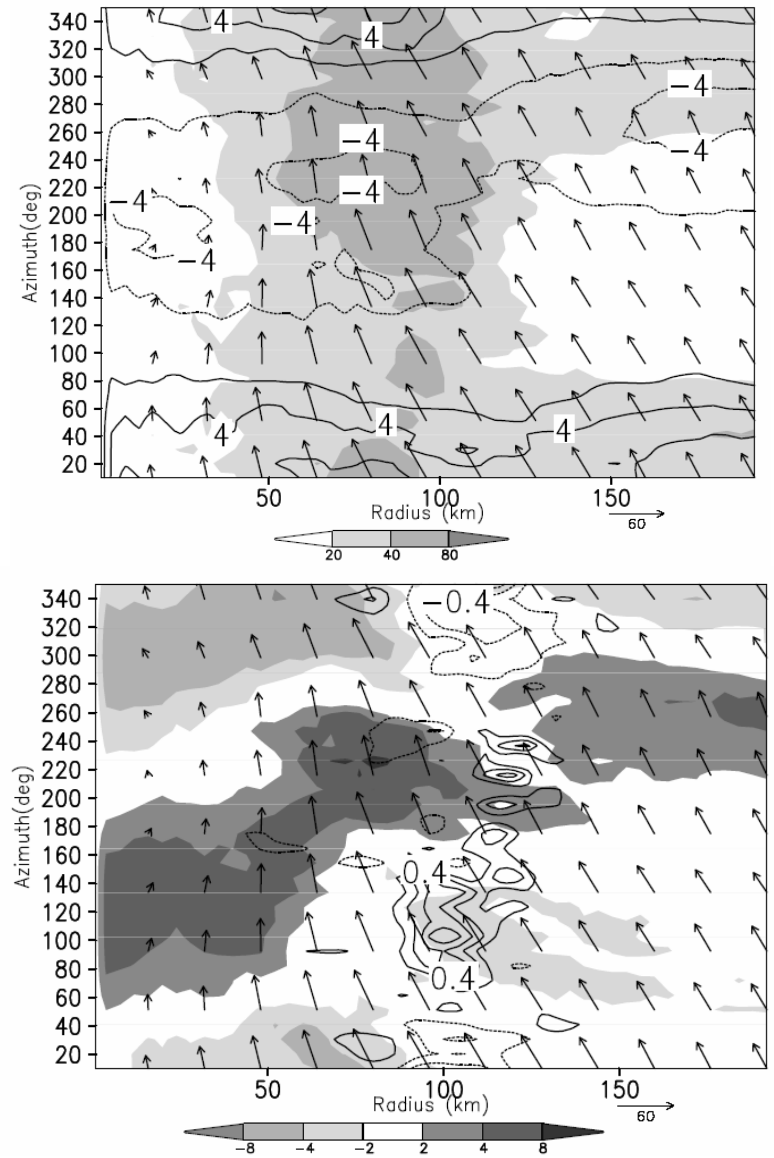

Figure 20: As in Fig. 19, for the 95 – 96 h simulation.

7. Conclusions

The current study has analyzed the energetic characteristics of Hurricane Bonnie (1998) using a high-resolution, explicit simulation. In a quasi-Lagrangian framework, energy equations have been derived in an effort to analyze Bonnie's evolution. It has been found that the evolution of volume-integrated KE is characterized by a constant increase, with the only decrease occurring coincident with an eyewall replacement cycle.

The volume-integrated LE, on the other hand, decreases until the onset of the eyewall replacement, after which time it increases until the end of the integration.

The structure of the KE is strongly affected by the vertical wind shear. Similar to the radar reflectivity, the KE exhibits a strong wavenumber-1 asymmetry on the downshear left side when the vertical shear is strong. Upon escaping the environment with high vertical shear, the KE evolves into an axisymmetric structure.

Mean and Eddy KE ($\overline{K}$ and K') equations have been derived in an effort to address the asymmetries and subsequent transition to axisymmetry. The problem of vortex tilting has been circumvented by restacking the vortex into an upright position prior to averaging. It is found that the evolution of K' is closely related to the vertical shear. In fact, the shear-generated asymmetries originate at the low-level eye-eyewall interface and propagate outward with time.

The K' budget shows that conversion from potential energy to K' dictates the evolution of K'. It is also found that while shear-forced asymmetries play a dominant role in the early development of Bonnie, the eyewall replacement cycle and later intensification is an almost exclusively axisymmetric process.

Appendix

Derivation of Equations for $\overline{K}$ and K’

The horizontal momentum equations in cylindrical and height coordinates are given by

$$\frac{du}{dt} = fv + \frac{v^2}{r} - \frac{1}{\rho}\frac{\partial p}{\partial r} + F_r \qquad \text{(A.1)}$$

$$\frac{dv}{dt} = -fu - \frac{uv}{r} - \frac{1}{r\rho}\frac{\partial p}{\partial \lambda} + F_\lambda \qquad \text{(A.2)}$$

where $\frac{d}{dt} = \frac{\partial}{\partial t} + u\frac{\partial}{\partial r} + \frac{v}{r}\frac{\partial}{\partial \lambda} + w\frac{\partial}{\partial z}$, and F_r and F_λ represent the frictional effects in the radial and azimuthal direction, respectively.

Multiplying (A.1) by u and (A.2) by v and then adding the resulting equations gives an equation for KE

$$\frac{dK}{dt} = -\frac{u}{\overline{\rho}}\frac{\partial p}{\partial r} - \frac{v}{r\rho}\frac{\partial p}{\partial \lambda} + uF_r + vF_\lambda \qquad \text{(A.3)}$$

Separating the velocity into mean and eddy components,

$u = U + u'$

$v = V + v'$

$w = W + w'$

and substituting into (A.1) and (A.2) yields

$$\frac{d(U+u')}{dt} = f(V+v') + \frac{(V+v')^2}{r} - \frac{1}{(\overline{\rho}+\rho')}\frac{\partial(\overline{p}+p')}{\partial r} + \overline{F_r} + F_r' \qquad \text{(A.4)}$$

$$\frac{d(V+v')}{dt} = -f(U+u') - \frac{(V+v')(U+u')}{r} - \frac{1}{r(\overline{\rho}+\rho')}\frac{\partial(\overline{p}+p')}{\partial \lambda} + \overline{F_\lambda} + F_\lambda' \qquad \text{(A.5)}$$

Taking the azimuthal average of (A.4) and (A.5),

$$\frac{dU}{dt} = fV + \frac{V^2 + \overline{v'v'}}{r} - \frac{1}{\overline{\rho}}\frac{\partial \overline{p}}{\partial r} + \overline{F_r} \qquad \text{(A.6)}$$

$$\frac{dV}{dt} = -fU - \left(\frac{UV + \overline{u'v'}}{r}\right) + \overline{F_\lambda} \qquad \text{(A.7)}$$

Multiplying (A.6) by U and (A.7) by V,

$$\frac{dU^2/2}{dt} = fUV + \frac{UV^2 + Uv'^2}{r} - \frac{U}{\overline{\rho}}\frac{\partial \overline{p}}{\partial r} + U\overline{F_r} \qquad \text{(A.8)}$$

$$\frac{dV^2/2}{dt} = -fUV - \frac{UV^2 + Vu'v'}{r} + V\overline{F_\lambda} \qquad \text{(A.9)}$$

And adding (A.8) and (A.9) gives an equation for the azimuthally averaged kinetic energy, K,

$$\frac{dK}{dt}=\frac{Uv'^{2}-Vu'v'}{r}-\frac{U}{\bar{\rho}}\frac{\partial\bar{p}}{\partial r}+U\overline{F_r}+V\overline{F_\lambda} \tag{A.10}$$

To derive an equation for K’ we begin with the equations for the momentum perturbations

$$\frac{du'}{dt}=fv'+\frac{2Vv'}{r}-\frac{1}{\bar{\rho}}\frac{\partial p'}{\partial r}+F_r' \tag{A.11}$$

$$\frac{dv'}{dt}=-fu'-\frac{(Vu'+Uv')}{r}-\frac{1}{\bar{\rho}r}\frac{\partial p'}{\partial\lambda}+F_\lambda' \tag{A.12}$$

And multiplying (A.11) and (A.12) by u’ and v’ respectively yields

$$\frac{du'^{2}/2}{dt}=fu'v'+\frac{2Vu'v'}{r}-\frac{u'}{\bar{\rho}}\frac{\partial p'}{\partial r}+u'F_r' \tag{A.13}$$

$$\frac{dv'^{2}/2}{dt}=-fu'v'-\frac{(Vu'v'+Uv'^{2})}{r}-\frac{v'}{\bar{\rho}r}\frac{\partial p'}{\partial\lambda}+v'F_\lambda' \tag{A.14}$$

Adding the above equations and azimuthally averaging yields a final equation for eddy kinetic energy, K’.

$$\frac{dK'}{dt}=\frac{V\overline{u'v'}-U\overline{v'v'}}{r}-\overline{\frac{u'}{\bar{\rho}}\frac{\partial p'}{\partial r}}-\overline{\frac{v'}{r\bar{\rho}}\frac{\partial p'}{\partial\lambda}}+\overline{u'F_r'}+\overline{v'F_\lambda'} \tag{A.15}$$

(A.15) can be represented symbolically as

$$\frac{dK'}{dt}=BTC+PTE+DISE \tag{A.16}$$

REFERENCES

Barnes, G. M., and Powell, M. D., 1995: Evolution of the Inflow Boundary Layer of Hurricane Gilbert (1988). *Mon. Wea. Rev.,* **123**, 2348–2368.

Braun, S. A., 2002: A Cloud-Resolving Simulation of Hurricane Bob (1991): Storm Structure and Eyewall Buoyancy. *Mon. Wea. Rev.,* **130**, 1573–1592.

Dudhia, J. 1993: A Nonhydrostatic Version of the Penn State–NCAR Mesoscale Model: Validation Tests and Simulation of an Atlantic Cyclone and Cold Front. *Mon. Wea. Rev.,* **121,** 1493–1513.

Frank, W. M., 1977: The Structure and Energetics of the Tropical Cyclone II. Dynamics and Energetics. *Mon. Wea. Rev.,* **105**, 1136–1150.

Kasahara, A., 1961: A Numerical Experiment on the Development of the Tropical Cyclone. *J. Atmos. Sci.,* **18**, 259–282.

Liu, Y., Zhang, D.-L., and Yau, M. K., 1997: A Multiscale Numerical Study of Hurricane Andrew (1992). Part I: Explicit Simulation and Verification. *Mon. Wea. Rev.,* **125**, 3073–3093.

McBride, J. L., 1981: Observational Analysis of Tropical Cyclone Formation. Part III: Budget Analysis. *J. Atmos. Sci.,* **38**, 1152–1166.

Ooyama, K., 1969: Numerical Simulation of the Life Cycle of Tropical Cyclones. *J. Atmos. Sci.,* **26**, 3–40.

Tuleya, R. E., and Kurihara, Y., 1975: The Energy and Angular Momentum Budgets of a Three-Dimensional Tropical Cyclone Model. *J. Atmos. Sci.,* **32** 287–301.

Wang, Y., 2002: Vortex Rossby Waves in a Numerically Simulated Tropical Cyclone. Part I: Overall Structure, Potential Vorticity, and Kinetic Energy Budgets. *J. Atmos. Sci.,* **59**, 1213–1238.

Vincent, D. G., Gommel, W. R., and Chang, L. N., 1974: Kinetic Energy Study of Hurricane Celia, 1970. *Mon. Wea. Rev.,* **102**, 35–47.

Zhu, T., D.-L. Zhang, and F. Weng, 2004: Numerical Simulation of Hurricane Bonnie (1998). Part I: Eyewall Evolution and Intensity Changes. *Mon. Wea. Rev.,* **132**, 225–241.